A Si-Micromachined 162-Stage Two-Part Knudsen Pump for On-Chip Vacuum

Seungdo An, *Member, IEEE*, Naveen K. Gupta, and Yogesh B. Gianchandani, *Fellow, IEEE*

***Abstract*— This paper investigates a two-part architecture for a Knudsen vacuum pump with no moving parts. This type of pump exploits the thermal transpiration that results from the free-molecular flow in nonisothermal channels. For a high compression ratio, 162 stages are serially cascaded. The two-part architecture uses 54 stages designed for the pressure range from 760 to ≈50 Torr, and 108 stages designed for lower pressures. This approach provides greater compression ratio and speed than using a uniform design for each stage. Finite element simulations and analytical design analysis are presented. A five-mask single-wafer fabrication process is used for monolithic integration of the Knudsen pump that has a footprint of 12 × 15 mm^2. The pressure levels of each stage are measured by integrated Pirani gauges. Experimental evaluation shows that, using an input power of ≈0.39 W, the evacuated chamber is reduced from 760 to ≈0.9 Torr, resulting in a compression ratio of ≈844. The vacuum levels are sustained during 37 days of continuous operation. [2013-0138]**

***Index Terms*— Micropump, Knudsen pump, thermal transpiration, two-part, multistage.**

I. INTRODUCTION

KNUDSEN pumps, first proposed and demonstrated in 1909 [1], present an appealing method for obtaining vacuum. These motionless pumps are based on the phenomenon of thermal transpiration [2]. If the hydraulic diameter of a flow channel is no larger than the mean free path of gas molecules (i.e., the flow in the channel is confined to the free-molecular or transitional flow regimes), a thermal gradient induces gas streams from the cold end to the hot end of the channel [2], [3]. Such a pumping method provides advantages over conventional motion-based pumping techniques. First, the absence of moving parts, without frictional loss and mechanical failure, provides significantly higher reliability. Second, this type of pump can potentially have a small form factor [4], [5]. Third, it can provide a high compression ratio using serially-cascaded configuration [1], [6], [7].

Microfabrication technology has been exploited for Knudsen pumps [4], [5], [7]–[14]. Miniaturized pumps are potentially useful for tunable vacuum control system in sealed cavities that contain high-Q resonators, such as micro gyroscopes [15] or timing oscillators [16]. Miniaturized analytical instruments, such as micro mass spectrometers [17], [18] and micro gas chromatographs [19]–[21], also need small vacuum pumps.

A monolithic Si implementation that used one stage was reported in 2005 and demonstrated a compression ratio of ≈2 [4]. The compression ratio can be increased to a limited extent by increasing the operating temperature. However, a more effective and scalable way to increase compression ratio is to cascade stages. Miniaturized multistage Knudsen pumps have been reported in the past [14], [22], but the early efforts were limited in scope because they did not utilize lithographic fabrication. In 2012, a monolithically fabricated 48-stage Knudsen vacuum pump was reported [7], resulting in a high compression ratio of 15 at atmospheric ambient pressure.

Together with the compression ratio, the pumping rate in a multistage Knudsen pump can be increased by adjusting the channel hydraulic diameter for the steady state operating pressure of each stage. An increased hydraulic diameter provides lower hydraulic resistance (i.e., higher pumping rate) as long as gas flow is confined to the free-molecular or transitional flow regimes for Knudsen pumping. The Knudsen pump described by Gupta *et al.* [7] used a uniform design for 48 stages, demonstrating the evacuation of on-chip cavities from 760 Torr to <50 Torr. The hydraulic diameter of the channels in this pump was designed to ensure the free-molecular or transitional flow at atmospheric pressure. For pumping to lower pressures, the hydraulic diameter of the upstream stages must be increased in order to increase the pumping rate. The compression ratio is not sacrificed because in steady state these upstream stages maintain relatively low cavity pressures at which the mean free path is much longer than at atmospheric pressure. However, the larger hydraulic diameter cannot sustain pumping in downstream stages. For this reason, a multistage Knudsen pump intended for a wide pressure range should be partitioned, so that both pumping rate and compression ratio can be enhanced for different parts of the pressure range.

In this context, this paper explores two-part customization of stages for a micromachined Knudsen pump.[1] Section II describes the two-part multistage architecture of a Knudsen pump, the heater design, and the Pirani pressure gauge. Section III details microfabrication processes and results. Test methods and results are presented in Section IV, followed by conclusions in Section V.

Manuscript received April 30, 2013; revised July 4, 2013; accepted August 1, 2013. This work was supported in part by the Microsystems Technology Office of the Defense Advanced Research Projects Agency High-Vacuum Program under Contract W31P4Q-09-1-0011. The work of S. An was supported in part by a fellowship from the Electrical Engineering and Computer Science at the University of Michigan. Subject Editor A. J. Ricco.

The authors are with the Department of Electrical Engineering and Computer Science, University of Michigan, Ann Arbor, MI 48109 USA (e-mail: sdan@umich.edu; gnaveen@umich.edu; yogesh@umich.edu).

Color versions of one or more of the figures in this paper are available online at http://ieeexplore.ieee.org.

Digital Object Identifier 10.1109/JMEMS.2013.2281316

[1]Portions of this work have been published in conference abstract form in [23].

This article has been accepted for inclusion in a future issue of this journal. Content is final as presented, with the exception of pagination.

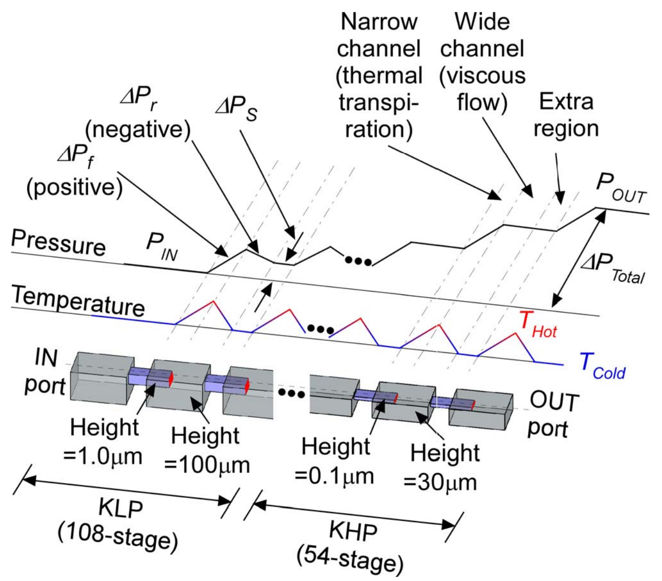

Fig. 1. Schematic of a two-part multistage Knudsen pump. KHP and KLP stages are serially cascaded. Temperature and pressure profiles are shown along the dashed line in stages. The dot-dash lines indicate correspondence along the flow path.

II. Design

A. Two-Part Multistage Architecture

Knudsen pumps combine thermal creep flow and viscous flow [2]. An imposed thermal gradient results in thermal creep flow along the channel walls from the cold end to the hot end. The pressure gradient induced by the thermal creep flow results in viscous flow in the reverse direction. The Knudsen number, defined as the ratio of the mean free path of gas molecules to the hydraulic diameter of a flow channel, is used to identify the relative contribution of the thermal creep flow and the viscous flow. In a narrow channel, if the Knudsen number is larger than ≈1, a pressure gradient is established in the same direction as the thermal gradient. This is the phenomenon of thermal transpiration. In contrast, a wide channel is dominated by viscous, pressure-driven (Poiseuille) flow (Fig. 1).

In a Knudsen pump, a single stage includes a narrow channel and wide channel. The narrow channel generates a forward pressure difference, ΔP_f, under the imposed thermal gradient along the intended forward path. In contrast, the wide channel, by connecting neighboring narrow channels, is intended to restore the temperature from the hot temperature, T_{Hot}, to the cold temperature, T_{Cold}, without a large drop in pressure. At equilibrium, the net pressure difference in a stage, ΔP_S, can be stated as:

$$\Delta P_S = \Delta P_f - \Delta P_r \tag{1}$$

where ΔP_r is the unintended, reverse transpiration pressure difference that could be developed in the wide channel at low pressures, at which the flow is not entirely viscous. A serial cascade increases the compression ratio; $\Delta P_{Total} = P_{OUT} - P_{IN} = \sum_i \Delta P_{S,i}$, where P_{OUT} and P_{IN} are the pressures at the OUT and IN ports, respectively, and i denotes the stage number.

The proposed two-part architecture (Fig. 1) is intended to enhance both pumping rate and compression ratio within an operating pressure range for each part. 1) The Knudsen high-pressure part (KHP), located downstream, is customized for the range from atmospheric pressure to 50 Torr. 2) The Knudsen low-pressure part (KLP), located upstream, is intended for the range from 50 Torr to sub-Torr pressure. The KHP and the KLP are comprised of serially cascaded single-stage Knudsen pumps, using 54 and 108 stages, respectively. The number of stages in the KLP is double that in the KHP, reflecting the larger compression ratio in the KLP than that in the KHP. In principle, the narrow and wide channels for each stage can be designed to provide the highest compression for the intended steady state operating conditions of that stage. However, this amount of dimensional diversity can significantly increase the manufacturing complexity. In this effort, two types of stage designs are pursued, as a compromise.

The following flow equation describes the volume flow rate of gas, $\dot{V}_X$, from the cold end to the hot end in a long rectangular channel [7], [24], [25]:

$$\dot{V}_X = \left(\frac{Q_T \Delta T}{T_{Avg}} - \frac{Q_P \Delta P}{P_{Avg}} \right) \frac{a^2 b P_{Avg}}{l} \sqrt{\frac{m}{2 k_B T_{Avg}}} \frac{1}{\rho_{Avg}} \tag{2}$$

where a, b, and l are, respectively, the height, width, and length of the channel; m is the mass of a single gas molecule; k_B is the Boltzmann constant; ΔT and T_{Avg} are, respectively, the temperature difference and the average temperature of T_{Cold} and T_{Hot}; ΔP and P_{Avg} are, respectively, the pressure difference and the average pressure of the cold and hot chambers; ρ_{Avg} is the mass density at P_{Avg} and T_{Avg}; and Q_T and Q_P are, respectively, the thermal creep flow and Poiseuille flow coefficients. Here, Q_P represents the viscous flow. Note that the terms in ΔT and ΔP have opposite signs to indicate that the viscous flow balances the thermal creep flow.

The values of Q_T and Q_P are obtained by Sharipov's calculation, which appropriately represents direct simulation Monte Carlo (DSMC) [26]. Sharipov [24] numerically solved the linearized Boltzmann transport equation (BTE), for extracting Q_T and Q_P from rarefied gas flow. Each flow coefficient was tabulated for the variations in ratio of a to b ($= a/b$), and the rarefaction parameter. The rarefaction parameter is defined as the inverse of Knudsen number, which is pressure-dependent. For parameters that are unlisted in [24], the values of Q_T and Q_P can be determined from interpolations of the tabulated values.

Instead of the volume flow rate, the standard flow rate, $\dot{V}_{Std}$, can be used to comprehend molecular flow through a multistage Knudsen pump where each stage is at a different pressure. To obtain $\dot{V}_{Std}$, the mass density, ρ_{Avg}, on the right side of Eq. (2), is substituted with the mass density at standard conditions, ρ_{Std}, provided by:

$$\rho_{Std} = \frac{m P_{Std}}{k_B T_{Std}} \tag{3}$$

where P_{Std} is the standard pressure of 760 Torr and T_{Std} is the standard temperature of 273.15 K. The standard flow rate allows easy comparison of molecular counts, whereas the volume flow rate is indicative of the swept volume. In Eq. (2), the subscript X in $\dot{V}_X$ denotes non-standard conditions defined by P_{Avg} and T_{Avg}. In a given narrow channel, as pressure decreases, the standard flow rate naturally decreases as well. However, the volume flow rate increases because Q_T increases relative to Q_P. This is reflected in Eq. (2) and (3).

The pressure difference across a channel, ΔP, depends upon the flow rate, as indicated in Eq. (2). When the pressure difference is zero (i.e., there is no pressure head), the flow rate takes the largest value. Over time, when evacuating a blind cavity, gas flow approaches equilibrium (i.e., no net flow), where the thermal creep flow due to ΔT is completely balanced by the viscous return flow due to ΔP. The resulting equilibrium pressure difference, ΔP_{Eq}, is given by:

$$\Delta P_{Eq} = \gamma \frac{\Delta T}{T_{Avg}} P_{Avg} \tag{4}$$

where γ is the flow coefficient ratio, defined as Q_T/Q_P, indicating the relative ratio of the thermal creep flow to Poiseuille flow coefficients in a channel [27]. In the free-molecular regime where the Knudsen number is larger than 10, γ takes its largest value of 0.5 for a/b ratio of 1 (square) to 0.44 for a/b of 0 (plate); in the viscous flow regime, where the Knudsen number is smaller than 0.01, γ takes its smallest value of 0 [24]. In the transitional regime, where the Knudsen number is between 10 and 0.1, γ is determined from [24] (Fig. 2a).

Using the determined γ values and Eq. (4), the values of ΔP_f for the narrow channel and ΔP_r for the wide channel at equilibrium are calculated. Hence, the net pressure difference in a stage, ΔP_S, as shown in Eq. (1), is directly proportional to the difference between the γ value for the narrow channel, γ_n, and that for the wide channel, γ_w. For a large value of γ_n, the narrow channel height is preferably no larger than the mean free path. In contrast, to achieve a small value for γ_w, the wide channel height is preferably much larger than the mean free path. In narrow channels of a fixed width, the pressure difference and the flow rate show opposite trends to the variation in channel height, a. Typically, a decrease in channel height, a, is accompanied by an increase in forward pressure difference, ΔP_f, and a decrease in standard flow rate, $\dot{V}_{Std}$, and vice versa.

B. Selection of Channel Dimensions

Channel dimensions selected for the narrow and wide channels are summarized in Table I. At 760 Torr, a narrow channel height of 0.1 μm in the KHP is similar to the N_2 mean free path of 0.07 μm (Table I); the resulting γ_n value of 0.22 provides a reasonable forward pressure difference in the narrow channel (Fig. 2a). At 50 Torr, the γ_n value in the KHP increases to 0.37. However, at 50 Torr, in the KLP, where the narrow channel height of 1 μm is similar to the mean free path of 1.12 μm, the resulting γ_n value is 0.27, which is smaller than the γ_n value of 0.37 for the KHP at the same pressure. While the loss in the ΔP_f due to the diminished γ_n value from 0.37 to 0.27 is small, the standard flow rate of 6×10^{-6} sccm at 50 Torr in the KLP is 30 times larger than 2×10^{-7} sccm at 50 Torr in the KHP and even 3 times larger

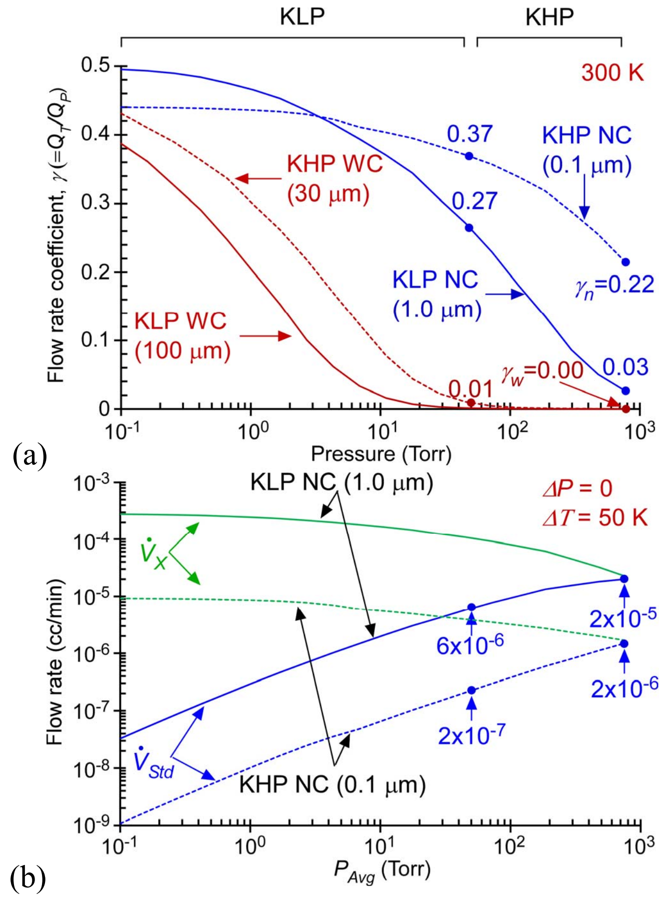

Fig. 2. Calculated flow parameters using the designed channel heights in Table 1. (a) Flow coefficient ratios, γ_n and γ_w, as a function of pressure. (b) $\dot{V}_X$ in cc/min and $\dot{V}_{Std}$ in sccm as a function of P_{Avg}, using Eq. (2) and (3). Narrow and wide channels, abbreviated as NC and WC, are indicated by the dotted and solid lines, respectively.

TABLE I
THE DESIGNED CHANNEL HEIGHTS, NUMBER OF STAGES AND THE MEAN FREE PATH, λ, OF N_2 GAS FOR KHP AND KLP IN A PRESSURE RANGE OF 760–0.1 TORR

Part	Narrow channel height (μm)	Wide channel height (μm)	Number of stages	Pressure (Torr)	λ (μm) at 300 K
KHP (760Torr -50Torr)	0.1	30	54	760	0.07
				200	0.28
				50	1.12
KLP (≤50Torr)	1.0	100	108	1	49
				0.1	511

than 2×10^{-6} sccm at 760 Torr in the KHP (Fig. 2b). The significantly larger value of the standard flow rate in the KLP is due to the quadratic dependence of the flow rate on the channel height, a, as shown in Eq. (2).

In the KHP, the wide channel height is 30 μm, considerably larger than the mean free path of 0.07 μm at 760 Torr; the γ_w value of 0.00 sufficiently suppresses the ΔP_r (Fig. 2a). In the KLP, the wide channel height is 100 μm, considerably larger

This article has been accepted for inclusion in a future issue of this journal. Content is final as presented, with the exception of pagination.

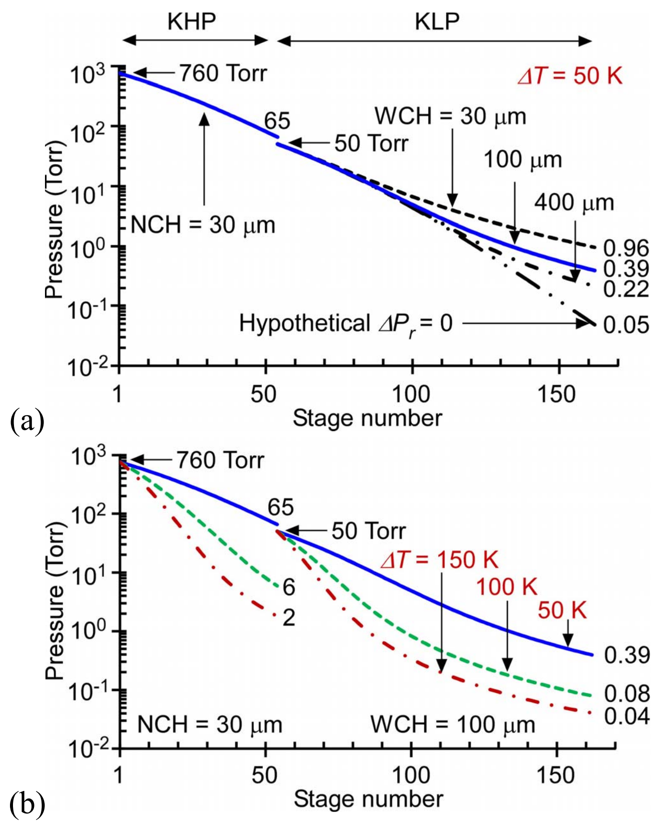

Fig. 3. Calculated equilibrium pressures at each stage. (a) Variation in wide channel height in the KLP, using the fixed ΔT of 50 K. (b) Variation in ΔT, using the fixed dimensions in Table I. Narrow and wide channel heights are abbreviated as NCH and WCH, respectively.

than the mean free path of 1.12 μm at 50 Torr. This reduces the magnitude of ΔP_r, as shown in the plots of γ_w (Fig. 2a). The wide channel height in the KHP is sized smaller than that in the KLP to reduce the dead volume represented by the wide channels, thereby resulting in faster pumping time with a negligible loss in suppressing the ΔP_r.

In this manner, the two-part design is accomplished by customizing the narrow channels for higher standard flow rate and the wide channels for smaller dead volume, while achieving high compression ratios in both KHP and KLP stages.

C. Calculated Equilibrium Pressures

The equilibrium pressures at each stage for the KHP and the KLP are theoretically calculated using Eq. (4) (Fig. 3). The intended design for the Knudsen pump (Table I) results in the upstream pressures of 65 Torr for the KHP and 0.39 Torr for the KLP, using ΔT of 50 K and T_{Cold} of 300 K (represented by blue solid lines in Fig. 3). All calculations assume that the KHP vents to a downstream pressure of 760 Torr, whereas the KLP has a downstream pressure of 50 Torr. The possible variations in wide channel height for the KLP and ΔT for both KHP and KLP are separately calculated as explained below.

First, using the fixed ΔT of 50 K, the effects of the increasing wide channel heights from 30 μm to 400 μm for the KLP on pressures are calculated (Fig. 3a). The upstream pressure for the KLP improves from 0.96 Torr for a wide channel height of 30 μm to 0.39 Torr for 100 μm, and further to 0.22 Torr for 400 μm. The hypothetical case in which ΔP_r is neglected is also plotted in Fig. 3a. This shows that the ΔP_r is increasingly noticeable at sub-Torr pressure as the wide channel height is decreased.

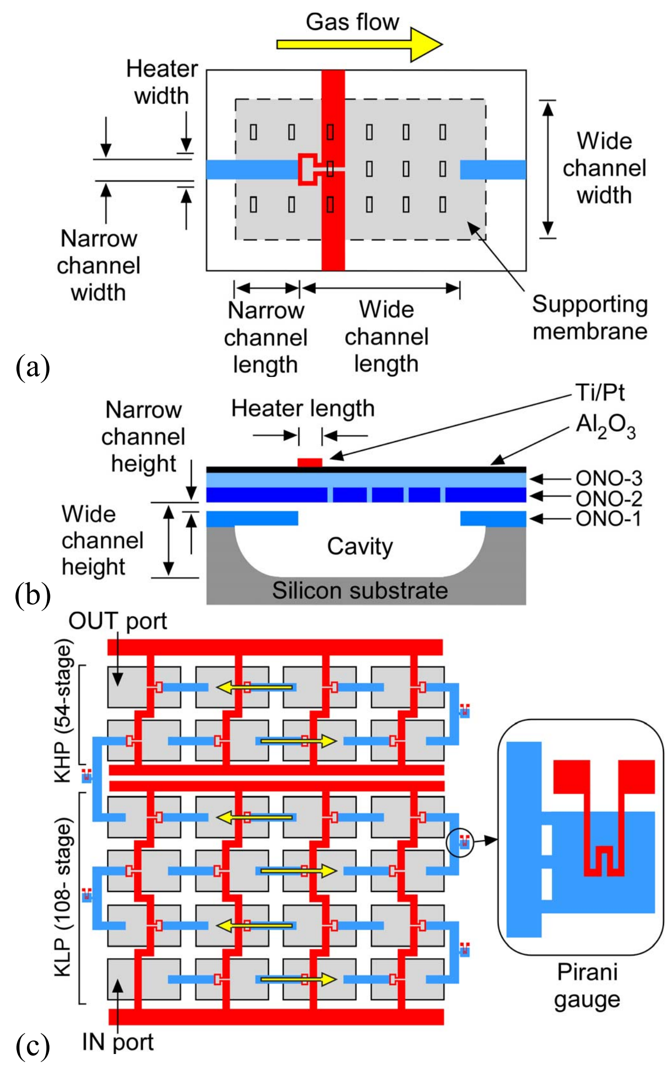

Fig. 4. (a) Representative layout of a single stage in a Knudsen pump. (b) Cross section along longitudinal axis. (c) Layout of overall KHP/KLP. In (c), the right side inset indicates a magnified view of a Pirani gauge.

Second, using the fixed channel dimensions listed in Table I, the effects of the increasing values of ΔT from 50 K to 150 K on pressures for both KHP and KLP are calculated (Fig. 3b). For the KHP, by increasing values of ΔT from 50 K to 100 K and to 150 K, the upstream pressure decreases from 65 Torr to 6 Torr and to 2 Torr, respectively. For the KLP, the upstream pressure decreases from 0.39 Torr to 0.08 Torr and to 0.04 Torr, respectively, but by smaller ratios than those for the KHP. The response for larger ΔT, especially at sub-Torr pressure, illustrates that the ability to reduce pressure by increasing ΔT is neutralized by ΔP_r.

D. Heater Design and Pirani Gauge

The layout of a single stage in the Knudsen pump is illustrated in Fig. 4. The narrow channel is formed by dielectric thin films located on the surface of the device, whereas the

This article has been accepted for inclusion in a future issue of this journal. Content is final as presented, with the exception of pagination.

TABLE II

DOE METHOD FOR LOW POWER HEATER DESIGN. TWELVE DESIGN FACTORS OF ARBITRARY LOW AND HIGH VALUES ARE USED TO FIND ΔT FOR AN INPUT POWER OF 2.4 mW. THE FOUR MAIN FACTORS, WHICH ARE BOXED, ARE FINE-TUNED FOR FINAL DIMENSIONS

Factors		Input 2-level Low (μm)	Input 2-level High (μm)	Output ΔT (K)	Final (KHP/KLP) (μm)
Wide channel	Width	300	400	-0.02	300
	Length	250	350	0.06	250
	Height	30	200	0.38	30/100
Narrow channel	Width	100	120	-0.05	22/12
	Length	30	200	9.23	100
	Height	0.1	0.2	0.04	0.1/1.0
Insulator thickness	ONO-1	1.2	1.5	-0.22	1.2
	ONO-3	1.3	3.8	-10.75	1.9
	Al_2O_3	0.0	0.5	-6.14	0.2
Heater	Length	25	50	-0.10	25
	Width	50	100	-3.72	25
	Thickness	0.1	0.2	-0.59	0.1

wide channel extends into a cavity in the wafer. A thin film metal trace serves as the heater integrated into each stage. The heater is suspended on a dielectric membrane at the boundary between the narrow channel and the wide channel. This location provides the maximum useful temperature gradient.

The input power for the Ti/Pt heater is minimized by increasing thermal isolation, using a design of experiments (DOE) method [28]. Using 12-factor, unpaired, 2-level DOE, finite element analysis (FEA) is performed, allowing each structural factor (parameter) to vary arbitrarily. Four primary dependencies are established by evaluating the impact on ΔT. The dimensions are then fine-tuned: 1) the narrow channel length; 2) the thickness of the oxide-nitride-oxide (ONO) layer (ONO-3); 3) the thickness of the Al_2O_3 layer; and 4) the heater width. For an imposed input power, a temperature increase for KHP can be regarded as similar to that for KLP because impacts of differences in height and width for the fabricated wide channel (described in Section III) are small, as can be seen from Table II. Using the final values in Table II, an input power of 2.4 mW can achieve 331.4 K if the lower surface of the device is held at 300 K (Fig. 5). For the 162-stage pump that is experimentally evaluated in Section IV, the resulting power is 0.39 W.

Integrated Pirani gauges, located adjacent to pump stages at the perimeter of the array, are used to measure the vacuum levels (Fig. 4c). The Pirani gauge converts pressure within a sense gap into a fractional change in electrical resistance of a localized Joule heater; this is caused by a change in the thermal

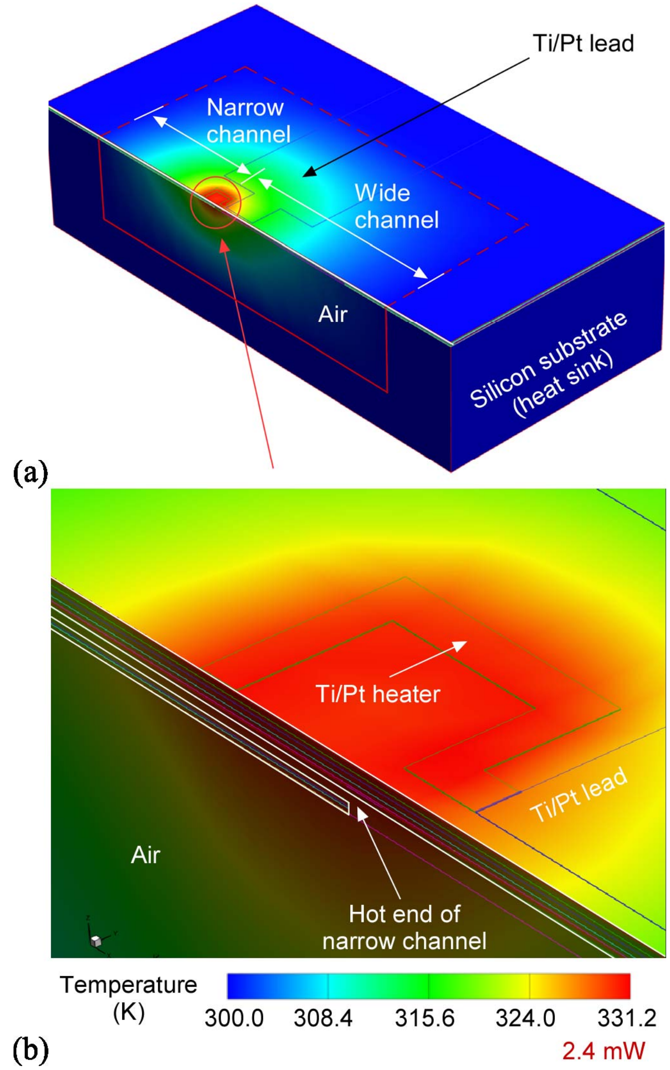

Fig. 5. Temperature distribution obtained by heater simulation of the designed KLP stage, using FEA. (a) Perspective view of a half-sliced single stage. (b) Magnified view of the T_{hot} position.

conductance change of the sense gap with pressure [29]. Four Pirani gauges, connected to stages 1, 54, 99, and 162, are selected for representing the pressure distribution in the overall KHP/KLP layout. These gauges are named P1, P54, P99, and P162, respectively. To enhance the sensitivity for a range from 760 Torr to 1 Torr, the sense gap is designed to be $\approx$1 μm [30]. This sense gap is identical to the narrow channel height in the KLP, so their fabrication steps are identical.

III. FABRICATION

To implement the Knudsen pump, a single-wafer five-mask fabrication process is used (Fig. 6). The important aspects in the channel fabrication are: 1) the narrow channels for the KHP are defined by a thin (sacrificial) polySi layer (Fig. 6b), whereas the narrow channels for the KLP are defined by both thin and thick (sacrificial) polySi layers (Fig. 6b, c); 2) cavities for wide channels are formed by partially etching the bulk silicon (Fig. 6e); and 3) the walls of the narrow channels are composed of stress-relieved oxide-nitride-

This article has been accepted for inclusion in a future issue of this journal. Content is final as presented, with the exception of pagination.

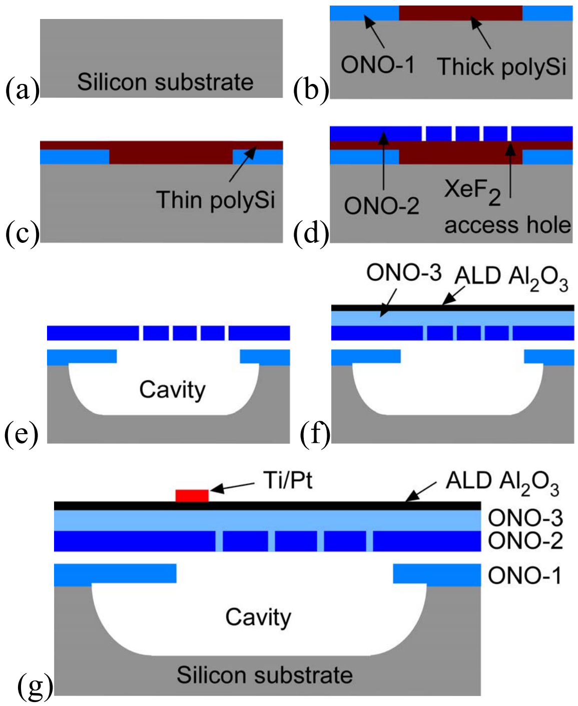

Fig. 6. The five-mask single-wafer process. (a) Silicon wafer. (b) Deposition and patterning of (Mask 1) LPCVD ONO-1 and (Mask 2) thick LPCVD polySi. (c) (Mask 3) Deposition & patterning of thin LPCVD polySi. (d) (Mask 4) Deposition and patterning of LPCVD ONO-2. (e) Sacrificial etching of polySi and bulk silicon using XeF_2 gas. (f) Deposition of PECVD ONO-3 and ALD Al_2O_3. (g) (Mask 5) Ti/Pt metallization.

TABLE III
MEASURED THICKNESS AND RESIDUAL STRESS OF EACH LAYER

Layer	Thickness (μm)	Residual stress (MPa)
LPCVD ONO-1	0.5/0.2/0.5	+42.5
LPCVD ONO-2	0.5/0.2/0.5	+42.5
PECVD ONO-3	0.7/0.5/0.7	+42.1
Thin / thick polySi	0.1 / 0.7	-
ALD Al_2O_3	0.2	+304
Ti/Pt	0.025/0.1	-

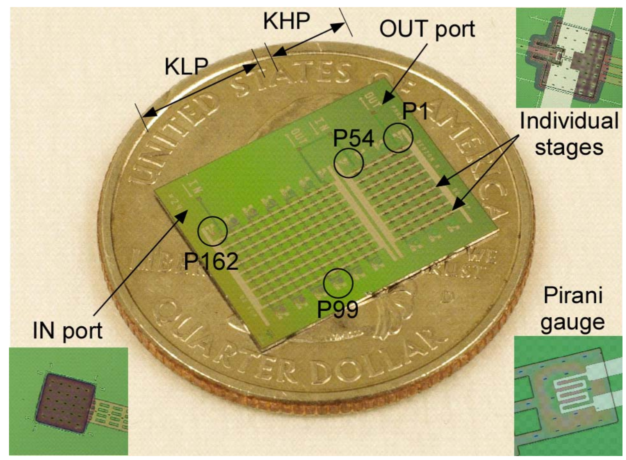

Fig. 7. Photograph of an as-fabricated chip. The upper right inset shows a stage, the lower right inset a Pirani gauge and the lower left inset the IN port.

oxide (ONO) layers. The (sacrificial) polySi layers are also used for hydraulic connections between KHP and KLP and between Pirani gauges and nearby stages.

The microfabrication process is initiated by deposition and patterning of the low-pressure chemical vapor deposited (LPCVD) first ONO layer (ONO-1) which is later used as a mask for the cavity etch of the single-crystal silicon substrate (Fig. 6a). The process continues with the deposition and patterning of a thick LPCVD polySi layer of $\approx$0.7 μm (Fig. 6b), followed by the deposition and patterning of a thin LPCVD polySi layer of $\approx$0.1 μm (Fig. 6c). After deposition of the LPCVD second ONO layer (ONO-2), an array of slits, 2×10 μm^2, are patterned using reactive ion etching (RIE); these are intended to provide XeF_2 access in the next step (Fig. 6d). Then, the sacrificial polySi layers are etched away by XeF_2 dry gas; the bulk silicon is partially removed in this step (Fig. 6e). The next step is to seal the access holes with the third ONO layer (ONO-3) that is $\approx$1.9 μm-thick. It is deposited by plasma-enhanced chemical vapor deposition (PECVD) because, with a deposition temperature of 380 °C, it provides lower thermal stress to the released membrane than LPCVD, which is typically performed at $>$800 °C. This is followed by a $\approx$0.2 μm-thick atomic layer deposited (ALD) Al_2O_3 layer that provides a hermetic seal (Fig. 6f). Finally, a metal layer of Ti/Pt (25/100 nm) is patterned, using lift-off process (Fig. 6g). This is used for heaters, Pirani gauges, and wire bonding pads.

At each step in the process, the thickness and residual stress of each layer are monitored (Table III). The oxide and nitride layers in each ONO layer are thickness-controlled to have a mild tensile residual stress of $\approx$42 MPa to avoid a buckling of the suspended membrane due to compressive residual stress. The total thickness of sacrificial polySi layers for the narrow channel in the KLP is $\approx$0.8 μm, lower than the design value of 1 μm in Section II. The fabricated chip has a footprint of 12×15 mm^2. The KHP, KLP, individual stages, IN/OUT ports, and Pirani gauges are shown in Fig. 7. The fabrication yield is typically 60–80% with the available tool set.

During fabrication, the main differences between the KHP and the KLP regions of the chip (Fig. 8) are: 1) the areal density of XeF_2 access holes is eight times larger in the KLP than that in the KHP; and 2) the narrow channels are formed by sacrificially etching the thin polySi layer for the KHP and the thin and thick polySi layers for the KLP. The height and the lateral undercut of the wide channel are controlled by the areal density of the XeF_2 access holes and etching time. Hence, the wide channel in the KLP is etched deeper than that in the KHP, and the XeF_2 lateral undercut profile in the KLP is wider than that in the KHP.

The cross sections of the narrow and wide channels in the KHP and the KLP are examined with scanning electron microscope (SEM) images (Fig. 9). The difference between the cross section of narrow channel in the KHP and KLP is evident from Fig. 9. The KHP uses a narrow channel that is 0.1 μm in height and 22 μm wide, whereas the KLP uses this, further enhanced by an opening that is nominally 0.8 μm in height and 12 μm wide. In the wide channel (Fig. 9c and d),

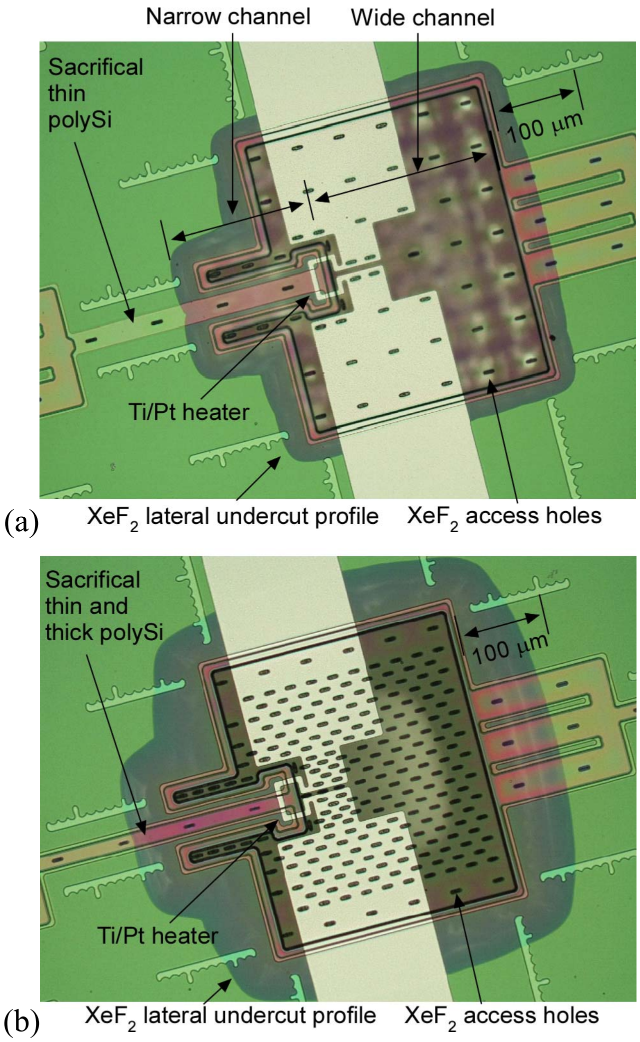

Fig. 8. Microscopic images of fabricated stages in an identical scale. (a) A KHP stage. (b) A KLP stage.

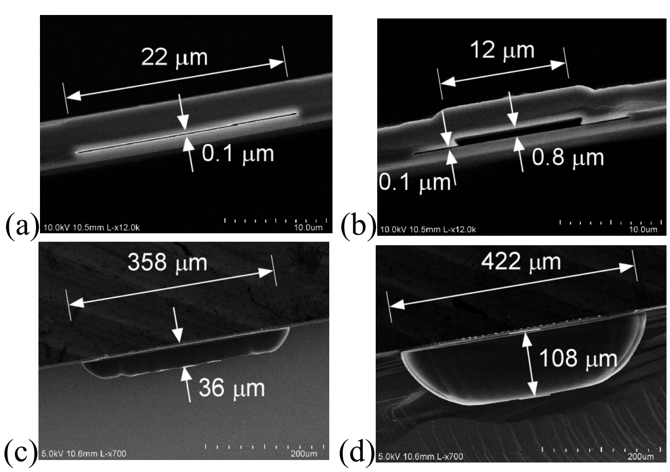

Fig. 9. SEM images of narrow and wide channels in KHP and KLP. (a) An narrow channel in KHP. (b) An increased narrow channel in KLP. (c) A wide channel in KHP. (d) An increased wide channel in KLP.

the eight times larger areal density of XeF_2 access holes in the KLP produces a height of 108 μm compared to that of 36 μm in the KHP. The larger density also produces a wider channel width of 422 μm in the KLP than that of 358 μm in the KHP, evident as the silhouette of the undercut in the top view (Fig. 8); the defined width of the cavity opening in the photomask (Fig. 6a) is only 300 μm in both KHP and KLP.

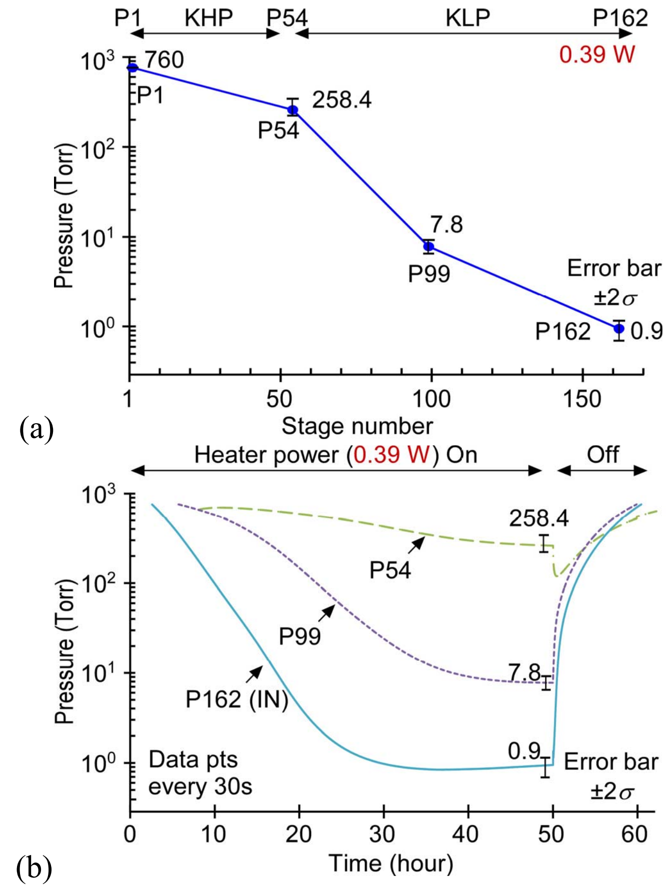

Fig. 10. Typical test results for the combined operation of KHP and KLP. (a) Equilibrium pressures at 760 Torr ambient. (b) Transient responses at 760 Torr ambient.

IV. Test Results

A. Methods

The fabricated chip is evaluated in a test chamber to permit the control of ambient pressure. The chip is wire-bonded for electrical connections from measurement tools to Ti/Pt metal pads. The substrate of the Knudsen pump is attached to a heat sink of the test chamber for thermally grounding to the room temperature in laboratory environment. The operating medium is laboratory air. The input port of the Knudsen pump is sealed, while the output port is open and vented to the test chamber. The pump is operated by providing a constant voltage to the Ti/Pt heater; the total input power to 162 stages is 390 mW and the input power in a stage is $\approx$2.4 mW. The temperature increase of the heater is calculated by dividing the fractional change in resistance by the thermal coefficient of resistance, α. The input power levels, as indicated in test results (Figs. 10–13), are for the heated resistances at equilibrium pressures.

For measuring the vacuum levels at evacuated stages, a constant current of 4 mA is provided to each Pirani gauge

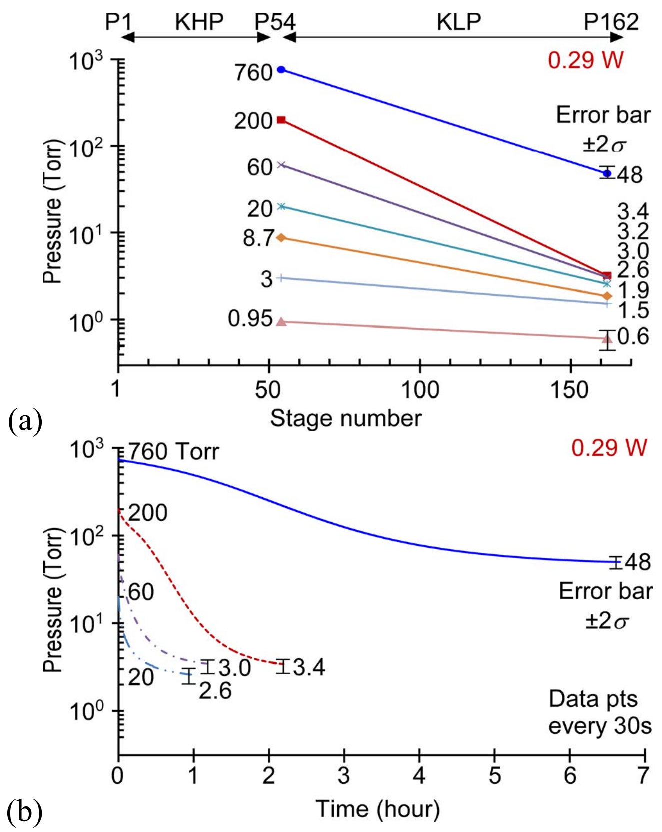

Fig. 11. Typical test results for the operation of KLP by itself. (a) Equilibrium pressures at various ambient pressures. (b) Transient responses of only P162 at each ambient pressure.

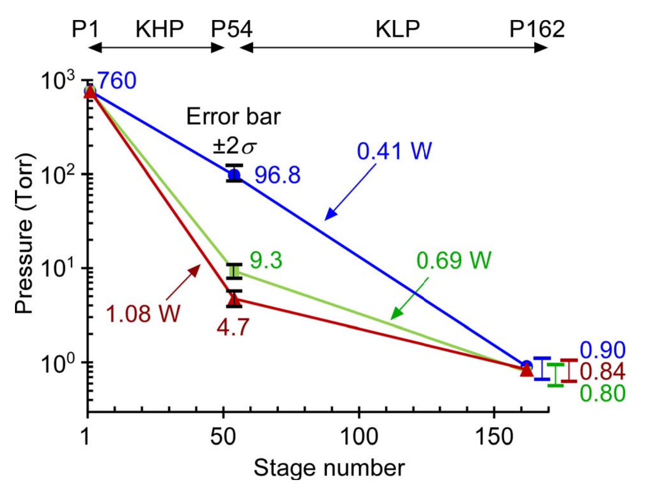

Fig. 12. Variation in input power for the combined operation of KHP and KLP at 760 Torr ambient.

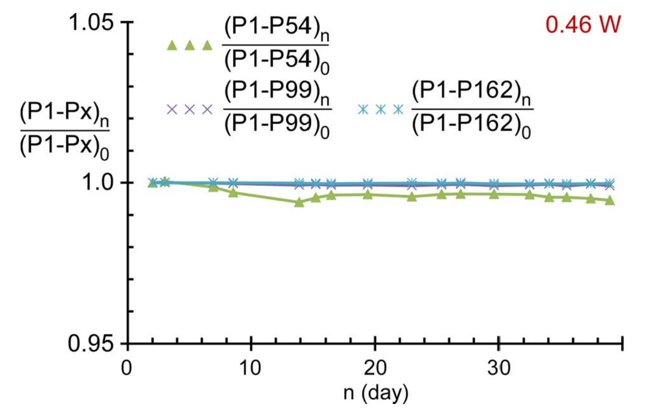

Fig. 13. Reliability test for 37 days of continuous operation. The subscript n denotes the elapsed days. Each pressure difference from Pirani gauge P1 to Pirani gauges P54, P99, and P162 is normalized to that at the beginning, *0*.

and the measured fractional change in resistance is correlated to pressure. The input power level for the heated resistance is ≈2.5 mW, which is modest relative to 390 mW for the Knudsen pump heater.

The Pirani gauges are calibrated by a special method, named dynamic calibration, which accommodates the reduced interior pressure and the ambient exterior pressure of the Pirani gauge during pump operation; this is described in [31] in detail. Here, the method is briefly illustrated for P162 and P1; P54, and P99 follow the case for P162. The method uses the response of P162 and P1 under rapid modulation of ambient pressure. 1) P162 provides a response that represents the combined effect of modulated exterior ambient pressure and nearly unchanged interior pressure; this is due to the relative slowness in pressure variation in the interior, as compared to the rapid modulation of the ambient pressure. 2) P1 provides a response that always represents the rapidly modulated ambient pressure because the interior, together with exterior, of P1 is directly exposed to ambient pressure. The multistep-modulation of the ambient pressure yields an equilibrium pressure for which the calibrated responses of P162 and P1 are equal. This equilibrium ambient pressure is exactly equal to the interior pressure of P162. Process-induced variations in responses of P162 and P1 are fitted by a linear regression model. In evaluating the pump performance, the measured pressure values are indicated with error bars for $\pm 2\sigma$ (where σ is the standard deviation), obtained by error analyses of the residual non-linearity in the regression model, together with repeatability of Pirani gauge sensors. The error bars for $\pm 2\sigma$ represent a 95.4% confidence interval, assuming normal (Gaussian) distribution [32].

B. Pumping Results

Two sets of tests are performed to evaluate the fabricated devices. The first test evaluates the combined operation of the KHP and KLP. For this test the inlet at stage 162 remains sealed, while stage 1 serves as the outlet. The second test evaluates the KLP by itself. For this test, stage 162 remains as the sealed inlet, while stage 54 serves as the outlet. In order to facilitate this, the supporting membrane at P54 is broken to allow it to vent to the ambient. Therefore, this is a destructive test.

The unheated resistances are ≈126 Ω for the Knudsen pump heater and ≈140 Ω for the Pirani gauge. The experimental value of α is 2,314 ppm/K for the Ti/Pt material used in both heaters and gauges. The temperature increase of the Pirani gauge from the typical fractional increase in resistance of 0.12 at 0.1 Torr is ≈52 K.

For the first set of tests (Fig. 10a), 0.39 W was applied to the heater at atmospheric ambient pressure. The temperature increase of the heater was typically ≈56 K; this increase is twice that of the theoretical estimate using FEA (Fig. 5). The pressure at P162 was 0.9 Torr, which corresponds to a total compression ratio of ≈844. The equilibrium pressures at intermediate stages were 258 Torr for P54 and 7.8 Torr for P99.

For the second set of tests (Fig. 11a), an input power of 0.29 W was applied. The temperature increase of the heater was typically ≈68 K. The equilibrium pressures of P162 were measured at various ambient pressures to mimic various downstream conditions for the KLP. At atmospheric pressure, the equilibrium pressure at P162 was 48 Torr. At ambient pressures from 200 Torr to 3 Torr, the equilibrium pressures ranged from 3.4 Torr to 1.5 Torr, respectively. At an ambient pressure of 0.95 Torr, the pressure reduced to 0.6 Torr.

The pre-equilibrium transient behavior was also evaluated during the two sets of tests. Using a Labview^{TM} program, the transient response was automatically recorded every 30 seconds after applying the input power. For the first set of tests at atmospheric ambient pressure, P162 took ≈25 hours to achieve equilibrium (Fig. 10b). P54 typically took ≈50 hours, i.e., twice as long. Once the heater was turned off, the pressure at P162 returned to the ambient value in ≈10 hours, 5 times shorter than the evacuation time of ≈50 hours for P54. The transient response for the second set of tests was measured at ambient pressures of 760 Torr, 200 Torr, 60 Torr, and 20 Torr (Fig. 11b). To achieve equilibrium, P162 took ≈5 hours, ≈2 hours, ≈1 hour, and ≈0.5 hour, respectively.

The impact of varying input power was investigated using the first set of tests at atmospheric ambient pressure (Fig. 12). The input power was increased to 0.41 W, 0.69 W, and 1.08 W. The temperature increases of the heater went up to ≈68 K, ≈120 K, and ≈174 K, respectively. The equilibrium pressures for P54 were 96.8 Torr, 9.3 Torr, and 4.7 Torr, respectively. The pressures for P162 were 0.90 Torr, 0.80 Torr, and 0.84 Torr, respectively. The highest compression ratio was approximately 760/0.80, i.e., 950, for 0.69 W. For the higher power of 1.08 W, the compression ratio was lower.

C. Reliability Tests

To investigate the reliability of a micromachined Knudsen pump, one sample of the full 162 stage Knudsen pump was continuously operated for 37 days, at an input power of 0.46 W. Figure 13 shows that the evacuation levels for each of Pirani gauges P54, P99, and P162 remained within 1% of the value on the first day. Since mechanical failure is unlikely because of the absence of moving parts, the primary failure mechanism could stem from the heating of the Knudsen pump. However, the thermal degradation of the various layers is expected to be very modest because the temperature increases by only 71 K, i.e., to about 96 °C, at 0.46 W. In contrast, the deposition temperature of the various thin films used in the fabrication were 910 °C for LPCVD oxide, 802 °C for LPCVD nitride, 380 °C for PECVD oxide, 380 °C for PECVD nitride, and 250 °C for ALD Al_2O_3. In case of Ti/Pt metal, annealing at 600 °C for 5 hours stabilizes electrical properties [33]. Hence, the Knudsen pump, without any substantial

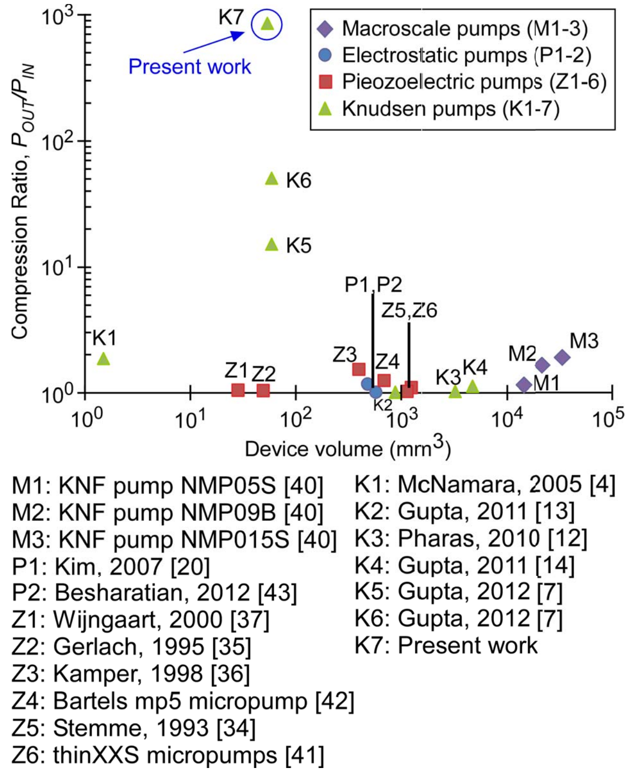

Fig. 14. Benchmarking with other pumps for compression ratio, P_{OUT}/P_{IN}, and device volume. The present work, for the combined operation of KHP and KLP, achieves a compression ratio of ≈844 (= 760/0.9), using an input power of 0.39 W. Note that, both x and y axes are log-scaled.

failure mechanism, can provide high reliability and long term operation.

V. Discussion and Conclusion

The compression ratio and device volume are benchmarked with other previously reported pumps [4], [7], [12]–[14], [20], [34]–[43]. Using an input power of 0.39 W, the compression ratio of ≈844 (= 760/0.9) exceeds the highest previous compression ratio [7], by a factor of ≈17, with 3.5 times better power efficiency (Fig. 14). This performance over the other pumps is enabled by: 1) the monolithic integration of 162 stages into one silicon chip, using silicon-based micromachining processes; 2) the two-part design, separately customizing stages into the KHP and the KLP; and 3) the heater design obtained by DOE and FEA.

The effect of ΔP_r at high vacuum was evident when using varying levels in input power (Fig. 12). For P162, the measured pressure remained between 0.9 Torr and 0.8 Torr without noticeable reduction, when the ΔT increased from 68 K to 174 K. In contrast, for a similar ΔT of 50 K to 150 K, the theoretically calculated pressure reduced from 0.39 Torr to 0.04 Torr, which is a larger ratio than that of the measurement. The measured results suggest that the unintended ΔP_r in the KLP wide channel fully neutralizes the ΔP_f in the narrow channel at pressures less than ≈1 Torr. For the theoretical calculation of Q_T and Q_P, it was assumed that T_{Hot} gradually decreases to T_{Cold} along the wide channel (Fig. 1). However, in the pressure range of 1 Torr to 0.1 Torr, the corresponding mean free path from 49 μm to 511 μm (Table I) encompasses the wide channel length of 250 μm. Therefore, air molecules could be transported from the hot to cold end without collision, resulting in hot molecules entering the cold end of the next narrow channel, and vice versa. This collisionless transport, which could break from the assumed gradual temperature change in the wide channel, could explain why the performance was less than predicted using theoretical calculations. For this reason, a more advanced level of design and experimentation at these low pressures is necessary for further improvement of compression.

The ΔP_r at high vacuum was also evident from the pressure response of P54. Using similar input powers of 0.39 W and 0.41 W (Figs. 10a, 12), the pressures of 258.4 Torr and 96.8 Torr at P54, respectively were reduced to $\approx$0.9 Torr at P162. The different pressures at P54 might be caused by sample-to-sample variations in channel dimensions. Figure 11 also shows similar P162 pressures of 3.4 Torr and 3.2 Torr when the initial pressures are different as 200 Torr and 60 Torr, respectively. It appears that the pressure at P54 bottoms near this level because of ΔP_r in the wide channel.

The pre-equilibrium transient behaviors at different levels of ambient pressure were consistent with the trends anticipated in Section II.A. For example, when the KLP was tested by itself, lowering the ambient pressure reduced the time needed for achieving equilibrium. Additionally, when the pump was tested as a whole, upstream stages achieved equilibrium before downstream stages.

In summary, a two-part (KHP and KLP) architecture has been investigated for the 162-stage Knudsen pump. A five-mask single-wafer process was used to fabricate the pump in a small footprint of 12 $\times$ 15 mm^2. Most notably, the high compression ratio of $\approx$844 was achieved at atmospheric ambient pressure; the input power was limited to $\approx$0.39 W; and the pump was reliable, with sustained operation over 37 days. Subsequent analyses suggest that at sub-Torr pressure ΔP_r in the wide channel neutralizes further evacuation. At the cost of additional masking steps in the fabrication process, the architecture may be extended to more than two partitions to improve pumping rate and compression ratio.

Acknowledgment

Facilities used for this research include the Lurie Nanofabrication Facility (LNF) operated by the Solid-State Electronics Laboratory (SSEL) and the University of Michigan.

References

[1] M. Knudsen, “Eine revision der gleichgewichtsbedingung der gase. Thermische molekularstromung,” *Annalen Phys.*, vol. 336, no. 1, pp. 205–229, 1909.
[2] L. Loeb, *The Kinetic Theory of Gases*. New York, NY, USA: McGraw-Hill, 1934, pp. 355–359.
[3] M. R. Cardenas, I. Graur, P. Perrier, and J. G. Meolans, “Thermal transpiration flow: A circular cross-section microtube submitted to a temperature gradient,” *Phys. Fluids*, vol. 23, no. 3, pp. 031702-1–031702-4, 2011.
[4] S. McNamara and Y. B. Gianchandani, “On-chip vacuum generated by a micromachined Knudsen pump,” *J. Microelectromech. Syst.*, vol. 14, no. 4, pp. 741–746, 2005.
[5] E. P. Muntz, M. Young, and S. E. Vargo, “Microscale vacuum pumps,” in *The MEMS Handbook*, 2nd ed., M. Gad-el-Hak, Ed. Boca Raton, FL, USA: CRC Press, 2006, ch. 8.
[6] R. M. Young, “Analysis of a micromachine based vacuum pump on a chip actuated by the thermal transpiration effect,” *J. Vac. Sci. Technol. B*, vol. 17, no. 2, pp. 280–287, 1999.
[7] N. K. Gupta, S. An, and Y. B. Gianchandani, “A Si-micromachined 48-stage Knudsen pump for on-chip vacuum,” *J. Micromech. Microeng.*, vol. 22, no. 10, pp. 105026-1–105026-8, 2012.
[8] E. P. Muntz, Y. Sone, K. Aoki, S. Vargo, and M. Young, “Performance analysis and optimization considerations for a Knudsen compressor in transitional flow,” *J. Vac. Sci. Technol. A*, vol. 20, no. 1, pp. 214–224, 2002.
[9] Y.-L. Han and E. P. Muntz, “Experimental investigation of micro-mesoscale Knudsen compressor performance at low pressures,” *J. Vac. Sci. Technol. B*, vol. 25, no. 3, pp. 703–714, 2007.
[10] N. K. Gupta and Y. B. Gianchandani, “Thermal transpiration in zeolites: A mechanism for motionless gas pumps,” *Appl. Phys. Lett.*, vol. 93, no. 19, pp. 193511-1–193511-3, 2008.
[11] S. Kosuge and S. Takata, “Database for flows of binary gas mixtures through a plane microchannel,” *Eur. J. Mech. B, Fluids*, vol. 27, no. 4, pp. 444–465, 2008.
[12] K. Pharas and S. McNamara, “Knudsen pump driven by a thermoelectric material,” *J. Micromech. Microeng.*, vol. 20, no. 12, pp. 125032-1–125032-7, 2010.
[13] N. K. Gupta and Y. B. Gianchandani, “Thermal transpiration in mixed cellulose ester membranes: Enabling miniature, motionless gas pumps,” *Microporous Mesoporous Mater.*, vol. 142, nos. 2–3, pp. 535–541, 2011.
[14] N. K. Gupta and Y. B. Gianchandani, “Porous ceramics for multistage Knudsen micropumps—Modeling approach and experimental evaluation,” *J. Micromech. Microeng.*, vol. 21, no. 9, pp. 095029-1–095029-14, 2011.
[15] K. Liu, W. Zhang, W. Chen, K. Li, F. Dai, F. Cui, X. Wu, G. Ma, and Q. Xiao, “The development of micro-gyroscope technology,” *J. Micromech. Microeng.*, vol. 19, no. 11, pp. 113001-1–113001-29, 2009.
[16] J. T. M. van Beek and R. Puers, “A review of MEMS oscillators for frequency reference and timing applications,” *J. Micromech. Microeng.*, vol. 22, no. 1, pp. 013001-1–013001-35, 2012.
[17] J. P. Hauschild, E. Wapelhorst, and J. Muller, “Mass spectra measured by a fully integrated MEMS mass spectrometer,” *Int. J. Mass Spectrometry*, vol. 264, no. 1, pp. 53–60, 2007.
[18] K. Cheung, L. F. Velasquez-Garcia, and A. I. Akinwande, “Chip-scale quadrupole mass filters for portable mass spectrometry,” *J. Microelectromech. Syst.*, vol. 19, no. 3, pp. 469–483, 2010.
[19] J. A. Potkay, G. R. Lambertus, R. D. Sacks, and K. D. Wise, “A low-power pressure- and temperature-programmable micro gas chromatography column,” *J. Microelectromech. Syst.*, vol. 16, no. 5, pp. 1071–1079, 2007.
[20] H. Kim, A. A. Astle, K. Najafi, L. P. Bernal, and P. D. Washabaugh, “A fully integrated high-efficiency peristaltic 18-stage gas micropump with active microvalves,” in *Proc. Int. Conf. MEMS*, 2007, pp. 127–130.
[21] J. Liu, N. K. Gupta, K. D. Wise, Y. B. Gianchandani, and X. Fan, “Demonstration of motionless Knudsen pump based micro-gas chromatography featuring micro-fabricated columns and on-column detectors,” *Lab Chip*, vol. 11, pp. 3487–3492, Aug. 2011.
[22] M. Young, Y. L. Han, E. P. Muntz, and G. Shiflett, “Characterization and optimization of a radiantly driven multi-stage Knudsen compressor,” in *Proc. AIP Conf.*, 2005, no. 762, pp. 174–179.
[23] S. An, N. K. Gupta, and Y. B. Gianchandani, “A monolithic 162-stage two-part Knudsen pump for high compression ratio,” in *Proc. Solid State Sensors, Actuat. Microsyst. Workshop*, 2012, pp. 14–17.
[24] F. Sharipov, “Non-isothermal gas flow through rectangular microchannels,” *J. Micromech. Microeng.*, vol. 9, no. 4, pp. 394–401, 1999.
[25] K. Jousten, *Handbook of Vacuum Technology*. New York, NY, USA: Wiley, 2008, ch. 5.
[26] N. D. Masters and W. Ye, “Octant flux splitting information preservation DSMC method for thermally driven flows,” *J. Comput. Phys.*, vol. 226, no. 2, pp. 2044–2062, 2007.
[27] F. Sharipov and V. Seleznev, “Data on internal rarefied gas flows,” *J. Phys. Chem. Ref. Data*, vol. 27, no. 3, pp. 657–706, 1998.
[28] J. Antony, *Design of Experiments for Engineers and Scientist*. Amsterdam, The Netherlands: Elsevier, 2003, ch. 2.
[29] C. H. Mastrangelo and R. S. Muller, “Microfabricated thermal absolute-pressure sensor with on-chip digital front-end processor,” *IEEE J. Solid-State Circuits*, vol. 26, no. 12, pp. 1998–2007, Dec. 1991.

[30] M. Doms, A. Bekesch, and J. Mueller, “A microfabricated Pirani pressure sensor operating near atmospheric pressure,” *J. Micromech. Microeng.*, vol. 15, no. 8, pp. 1504–1510, 2005.

[31] S. An and Y. B. Gianchandani, “A dynamic calibration method for Pirani gauges embedded in fluidic networks,” *J. Microelectromech. Syst.*, to be published, DOI: 10.1109/JMEMS.2013.2281319.

[32] E. Kreyszig, *Advanced Engineering Mathematics*, 9th ed. New York, NY, USA: Wiley, 2006, pp. 1049–1057.

[33] W. Qu, W. Wlodarski, and M. Austin, “Microfabrication and reliability study of sapphire based Ti/Pt-electrodes for thin-film gas sensor applications,” *Microelectron. J.*, vol. 31, no. 7, pp. 561–567, 2000.

[34] E. Stemme and G. Stemme, “A valveless diffuser/nozzle-based fluid pump,” *Sens. Actuators A, Phys.*, vol. 39, no. 2, pp. 159–167, 1993.

[35] T. Gerlach and H. Wurmus, “Working principle and performance of the dynamic micropump,” *Sens. Actuators A, Phys.*, vol. 50, no. 1, pp. 135–140, 1995.

[36] K. P. Kamper, J. Dopper, W. Ehrfeld, and S. Oberbeck, “A self-filling low-cost membrane micropump,” in *Proc. IEEE Int. Conf. MEMS*, Jan. 1998, pp. 432–437.

[37] W. Wijngaart, H. Andersson, and P. Enoksson, “The first self-priming and Bi-directional valve-less diffuser micropump for both liquid and gas,” in *Proc. IEEE Int. Conf. MEMS*, Jan. 2000, pp. 674–679.

[38] N.-T. Nguyen, X. Huang, and T. K. Chuan, “MEMS-micropumps: A review,” *Trans. ASME J. Fluids Eng.*, vol. 124, no. 22, pp. 384–392, 2002.

[39] D. J. Laser and J. G. Santiago, “A review of micropumps,” *J. Micromech. Microeng.*, vol. 14, no. 6, pp. R35–R64, 2004.

[40] R. Kach and C. Kissling, “Diaphragm pump,” U.S. Patent 7 373 872, May 20, 2008.

[41] L. Weber, “Micropump and method for the production thereof,” U.S. Patent 7 771 176, Aug. 10, 2010.

[42] R. Meyknecht, “Micropump and adhesive-free method for joining two substrates,” U.S. Patent 8 043 073, Oct. 25, 2011.

[43] A. Besharatian, K. Kumar, R. L. Peterson, L. P. Bernal, and K. Najafi, “A scalable, modular, multi-stage, peristaltic, electrostatic gas micropump,” in *Proc. IEEE Int. Conf. MEMS*, Jan./Feb. 2012, pp. 1001–1004.

Seungdo An (S’12–M’13) received the B.S. and M.S. degrees in chemistry from Korea University, Seoul, Korea, in 1995 and 2003, respectively. He worked at Samsung, Korea, from 1995 to 2010. At Samsung, he was involved in various MEMS projects, including micro gyroscope, micro magnetometer, and laser optical modulator/display. He was a Visiting Researcher at the Esashi Laboratory, Tohoku University, Sendai, Japan, in 1996. Since 2010, he has been pursuing the Ph.D. degree in electrical engineering at the University of Michigan, Ann Arbor, MI, USA, with a focus on MEMS. His academic advisor is Prof. Gianchandani.

His research interests are monolithic Knudsen vacuum pumps for micro gas chromatographs and micro mass spectrometers.

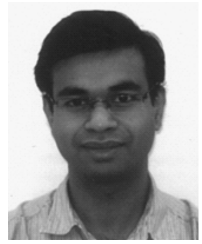

Naveen K. Gupta was born in Kanpur, India. He received the B.Tech. degree in mechanical engineering from the Indian Institute of Technology Kanpur, Kanpur, in 2004. He was a Maintenance Engineer for the Hindustan Petroleum Corporation Ltd., Chennai, India, from 2004 to 2005. He received the M.S. and Ph.D. degrees in mechanical engineering from the University of Michigan, Ann Arbor, MI, USA, in 2009 and 2010, respectively. His thesis was one of the leading efforts toward the design and development of Knudsen pumps with high gas flow rates (≈1 sccm) operating at atmospheric pressure. Knudsen pumps are of particular interest because they do not have any moving parts and their effectiveness increases with miniaturization. He was a Postdoctoral Research Fellow at the University of Michigan from 2010 to 2011. As a Postdoctoral Research Fellow, he pioneered the development of a single-chip multistage pump for high vacuum pumping applications. He was also involved in exploring the possibility of using Knudsen pumps for gas chromatography.

Yogesh B. Gianchandani (M’85–SM’05–F’10) is a Professor at the University of Michigan, Ann Arbor, MI, USA, with a primary appointment in the Electrical Engineering and Computer Science Department and a courtesy appointment in the Mechanical Engineering Department. He also serves as the Director for the Center for Wireless Integrated MicroSensing and Systems ($WIMS^2$).

Dr. Gianchandani’s research interests include all aspects of design, fabrication, and packaging of micromachined sensors and actuators (http://www.eecs.umich.edu/∼yogesh/). He has published about 300 papers in journals and conferences, and has about 35 U.S. patents issued or pending. He was a Chief Co-Editor of *Comprehensive Microsystems: Fundamentals, Technology, and Applications*, published in 2008. From 2007 to 2009, he also served at the National Science Foundation, as the Program Director for Micro and Nano Systems within the Electrical, Communication, and Cyber Systems Division (ECCS). Dr. Gianchandani is a Fellow of the IEEE.